DETECTOR TEMPERATURE DEPENDENCE OF THE 12 MICRON CHANNEL FILTER PROFILE AND ITS IMPACT ON THE ATSR-1 CALIBRATION

A.R. Birks

October 2008

RUTHERFORD APPLETON LABORATORY

Chilton, Didcot,

Oxfordshire OX11 0QX, U.K.

SCIENCE AND TECHNOLOGY FACILITIES COUNCIL

Revision Record

Date	Issue	Details
29/10/2008	1.0	Initial release

Table of Contents

DETECTOR TEMPERATURE DEPENDENCE OF THE 12 MICRON CHANNEL FILTER PROFILE AND ITS IMPACT ON THE ATSR-1 CALIBRATION

1 Introduction

Among the factors that contribute to the excellent performance and sensitivity of the ATSR series of instruments is the use of low-noise infra-red detectors that are cooled to low temperature by means of a mechanical Stirling cycle cooler.

The infra-red detectors on the ATSR series instruments are designed to be operated at a temperature of around 80 K, in order to maximise their sensitivity and noise performance, and it is the purpose of the Stirling cycle cooler to maintain this temperature. However, in the case of ATSR-1, the performance of the cooler deteriorated in the latter part of the mission. Initially the ATSR-1 on-board cooler reached a cold block temperature of 89 ± 1 K, but from early 1994 it proved increasingly difficult for the cooler to maintain the detector temperatures below their optimum of 95 K and so, to reduce mechanical wear and maximise the life of the cooler, temperatures were allowed to rise gradually, and reached 110 K in early 1996. Figure 1 shows the effect.

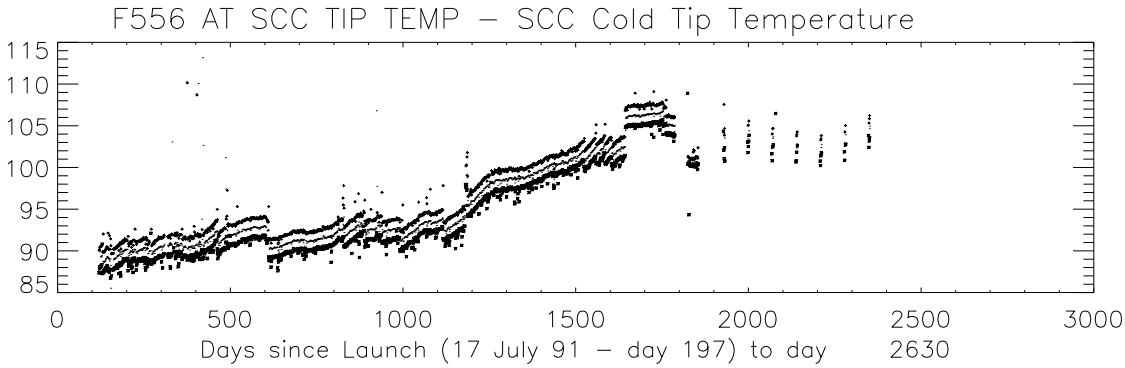

Figure 1. Variation of ATSR-1 detector temperature during the mission.

An effect of this warming is to modify the spectral response of the 12 micron detector; although the other detectors may be affected to some degree, only in the case of the 12 micron channel is the spectral response significantly altered. The effect is to modify the long-wavelength cut-off. This in turn affects the calibration and the retrieved SSTs [**1**].

The calibration of the channel, and the determination of the retrieval coefficients, both separately depend on the channel response (which is a factor in the temperature to radiance conversion, and in the atmospheric modelling). Therefore use of coefficients derived from an erroneous spectral response will give rise to errors in the retrieval. In order to eliminate bias in the retrieved SSTs. we need to account for this effect. The simplest way to do so is to re-process with both temperature to radiance conversion tables and retrieval coefficients re-derived to account for the elevated detector temperature.

An initial discussion of this effect was given by the present author [**2**], from which some of the material in this report is derived. This report updates the work in that reference, and derives profiles that can enable the uncertainties in the modelling of this effect due to the limited number of available detector samples to be characterised.

2 Dependence of Instrument Characteristics on Detector Temperature

2.1 The physics of the detector

The long-wavelength (11 and 12 micron) channels of ATSR use photoconductive detectors made from n-doped Mercury Cadmium Telluride (HgCdTe). This material is a semiconductor whose properties make it extremely suitable for use as a detector in the mid to long wavelength infra-red [**3**]. Photons incident on the material will excite electrons from the valence band to the conduction band, thus increasing the number of conduction electrons and hence the conductivity. If the device is biased at constant current, the resultant change in conductivity appears as a change in the voltage across the detector, which can be measured. (The doping is to provide a baseline level of conductivity to allow the device to be current biased.)

HgCdTe is an alloy of HgTe and CdTe, and can be represented by the stoichiometric formula $Hg_{1-x}Cd_xTe$, where the composition parameter x represents the fraction of CdTe in the mixture. Pure CdTe is a semiconductor with a band gap (the energy gap between the conduction and valence bands) of about 1.6 eV, whereas HgTe is a semimetal; that is to say, the conduction and valence bands overlap, and there is no band gap. When the two are mixed, the resultant alloy has a band gap intermediate between these extremes, the size of which can be varied by varying the composition.

Several formulae have been proposed to represent the size of the band gap as a function of composition and temperature. One of these, attributed to Kruse [**4**] and cited by Mason [**5**] is

$$E_g = -0.25 + 1.59x + 0.327x^3 + 5.233\times10^{-4}(1 - 2.08x)T\,, \qquad (2.1)$$

where E_g is the band gap in electron volts, x is the alloy composition ratio defined above, and T is the absolute temperature of the material in K. An alternative equation was derived by Hansen et al [**6**]:

$$E_g = -0.302 + 1.93x - 0.81x^2 + 0.832x^3 + 5.35\times10^{-4}(1 - 2x)T\,. \qquad (2.2)$$

Figure 2 shows the band gap derived from Equation 2.2 plotted for two temperatures T = 80 K and T = 90 K.

If it is to excite an electron into the conduction band, an incident photon must have energy greater than the band gap E_g. This condition sets the cut-off wavelength such that photons of longer wavelength have insufficient energy to promote an electron.

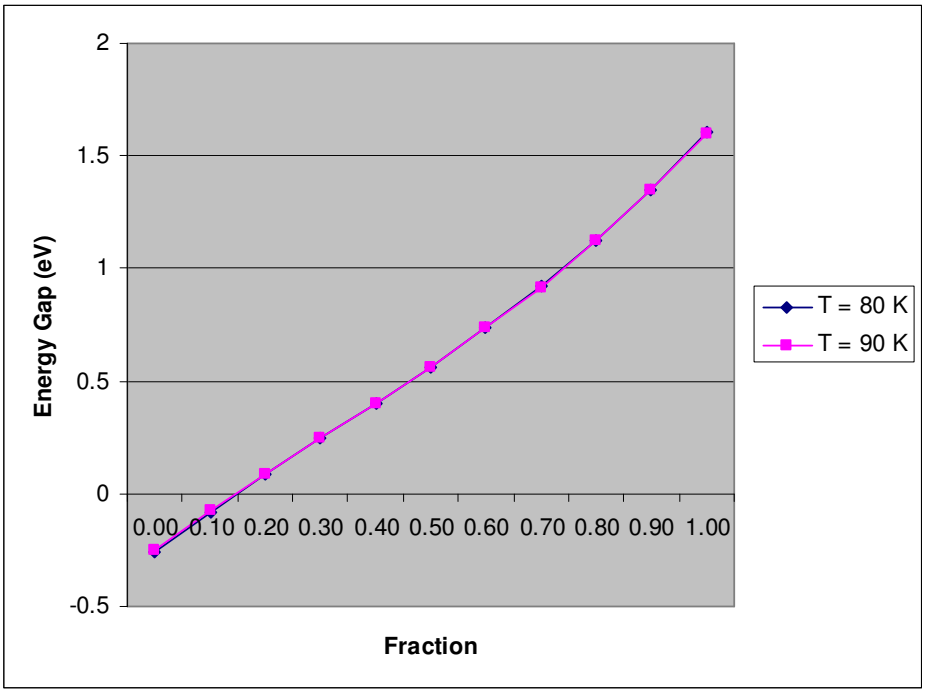

Figure 2: Band Gap for HgCdTe plotted as a function of composition ratio x (based on Reference [6])

The cut-off wavelength λ at which the photon energy equals E_g is given by

$$hc/\lambda = eE_g \quad \text{or} \quad \lambda = hc/eE_g \tag{2.3}$$

where h is Planck's constant, c is the velocity of light, and e is the magnitude of the charge on the electron (if E_g is expressed in eV, eE_g is the energy gap in Joules). At longer wavelengths the material is transparent. The cut-off wavelength thus defines the longest wavelength at which the material will function as a detector, and its dependence on x means that this limit can be tailored to the desired spectral band-width of the detector by varying the composition of the alloy.

Measurements by Mullard (reported by Mason [**5**]) determined the composition values of the ATSR-1 flight detectors to be $x = 0.194$ and $x = 0.195$ for the 10.8 and 12 micron channels respectively[1]. Substituting these values in equation (2.1) we find cut-off wavelengths of 14.34 and 14.09 microns respectively at 82K.

Equations (2.1) and (2.2) both show that the band gap is temperature dependent, with a temperature coefficient at x = 20% of the order of 3×10^{-4} eV/K. The sign of the dependence is such that the band gap increases with increasing temperature, so that the cut-off wavelength moves to shorter wavelengths as temperature increases. The long wavelength cut-off of the 12 micron channel is not defined by the cut-off wavelength of the material (it is limited to about 13.5 microns by a filter within the FPA), nevertheless, the responsivity of the material to incident photons does not cut off discontinuously at the cut-off wavelength, but will show some fall-off as the cut-off wavelength is approached. Increasing temperature will have the qualitiative effect

[1] These figures are cited at one point in Reference [5] as 1.94 and 1.95 respectively, but these values are obviously unphysical, since x cannot exceed unity. It is clear that the decimal point has been misplaced, and this is confirmed elsewhere in the reference.

of moving the response curve to shorter wavelengths, with corresponding effect on the channel profile.

2.2 Focal Plane Assembly

The spectral profiles of the AATSR channels are primarily determined by the optical properties of the Focal Plane Assembly (FPA).

Descriptions of the FPA can be found in references [**5**] and [**8**]. Briefly, the entrance aperture of the FPA coincides with the focal plane of the primary mirror of the ATSR fore-optics. The field stop that defines the ATSR pixel is positioned here. Radiation passing through the field stop is segregated into channels by a series of three dichroic beam-splitters. The first two of these divert the 1.6 micron and 3.7 micron bands to their respective detectors, while the final beam splitter separates the 10.8 and 11 micron bands. Following each beam splitter an ellipsoidal mirror, or in the case of the 1.6 micron channel, an aspheric lens, images the field stop in that channel onto its respective detector. A multi-layer filter is placed in front of each detector to define the channel profile.

In the particular case of the 12 micron channel, the overall transmission profile of the FPA will be predominantly defined by the combined effects of the final beam splitter and the filter placed in front of the detector. The short-wavelength edge of the profile will be defined by the beam splitter, falling as more radiation is diverted to the 10.8 micron detector as wavelength is reduced. The long-wavelength edge is limited by the channel filter.

The overall sensitivity of the channel to incident radiation will be the combined effect of the transmission of the of the optical path in the FPA, and the response of the detector to incident photons.

Thus for any detector temperature T, we can write the overall profile of the ATSR-1 channel, as a function of wavelength, as

$$\varphi_\lambda(\lambda,T) = t_0(\lambda)t_1(T,\lambda) \tag{2.4}$$

where t_0 represents the optical transmission of the FPA at wavelength λ, including the dominant components of the beam splitter at the shorter wavelengths, and of the channel filter at longer wavelengths, and t_1 represents the response of the photoconductive detector material as a function of detector temperature and wavelength. Note that following Mason [**5**] we are using λ as a suffix to distinguish the ATSR channel under consideration, independently of its use as the independent variable of the profiles. Thus the LHS of equation (2.4) represents the profile of channel λ as a function of wavelength λ.

We assume that the optical transmission in independent of detector temperature T. The issue, then, is to characterise the detector response t_1.

3 Characterisation of the ATSR 12 micron Detectors

3.1 Measurements of Flight Spare Detectors

No measurements showing the behaviour of the actual flight detectors of ATSR-1 were made prior to launch. By the time the problem was identified, it was already too late to characterise the flight detector, as it was in space. Therefore in order to quantify the effects of detector temperature on performance, measurements were made of flight spare detectors post-launch, it being assumed that these were representative of the flight detector.

These measurements were made by the manufacturers of the detectors, Mullard Ltd., in November 1991 (J. Delderfield, private communication) and showed the relative spectral response of the flight spare detectors at temperatures spanning the range 80 to 110 K.

Measurements were made on two detector elements, designated M03 and M09, and for each detector, measurements of relative spectral response as a function of wavelength were made at each of the 9 temperatures in Table 1 below.

Table 1.

Measured detector temperatures (K)						
80.0	85.0	90.0	95.0	100.0	105.0	110.0

For each temperature the measured data consists of a series of measurements of relative spectral response at 66 wavelengths spaced by approximately 0.1 micron intervals between 7.002 and 13.502 microns.

Figure 3 shows the measurements on the flight spare detector M03. The figure shows the quantitative effect of the temperature change; the change of the long wavelength edge is clear. The edges of the detector response move to shorter wavelength as temperature increases. The effect is greater at the long wavelength (low wave number) edge. Moreover the overall response of the 12 micron channel is dominated at the high wave number edge by the spectral response of the beam splitter that separates the channels. Thus the net effect is to modify the low frequency (long-wavelength) cut-off of the channel spectral response.

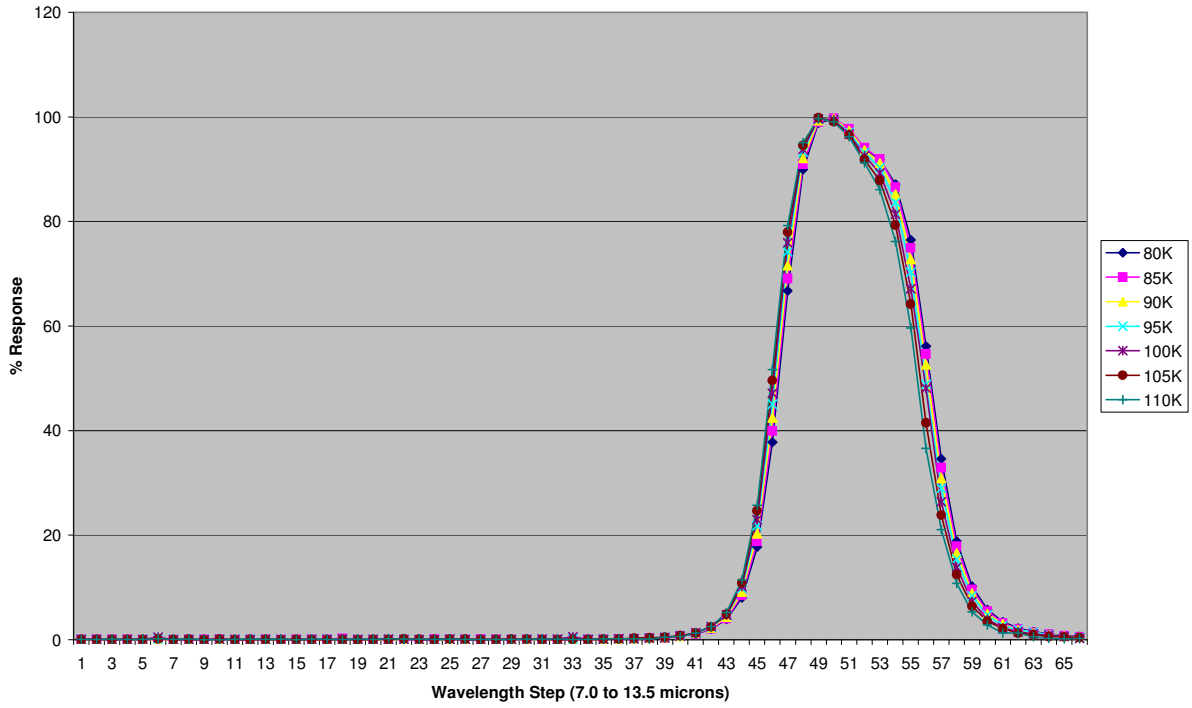

Figure 3: Measured variation of the frequency response of flight spare detector M03 at 7 temperatures.

3.2 Derivation of Modified Filter Profiles

Measurements such as those in Figure 3 cannot be used directly to characterise the on-board profile, because what is measured in each case is the combined effect of the response function of the detector and the transmission of the optical path.

The measurements show the product of the spectral response function of the detector and the profile of the filters in the measurement setup. To characterise the temperature dependence of the detector response, we must separate the temperature dependent component from the optical transmission profile of the measurement setup. By taking the ratio of the measurement at each detector temperature to that at some reference temperature, we can eliminate the effects of the measurement setup and define the detector response functions relative to that at the reference temperature, which we take to be 82 K, being the temperature at which the ground calibration took place.

The resulting ratio can be applied to the on-board filter profile measured during ground calibration to derive the modified profile of the instrument for any elevated detector temperature.

By analogy with Equation (2.4), we can write

$$\varphi_{meas}(\lambda,T) = t_2(\lambda)t_1(T,\lambda) \qquad (3.1)$$

where φ_{meas} is the relative spectral response of the detector in the measurement configuration, t_2 represents the optical transmission of the measurement configuration at wavelength λ, and t_1 represents the response of the photoconductive detector material as a function of detector temperature as before.

The analysis is perhaps clearer if we work with logarithms. From (3.1)

$$\log \varphi_{meas}(\lambda,T) = \log t_2(\lambda) + \log t_1(\lambda,T) \qquad (3.2)$$

If we select a reference temperature T_{ref}, we can write

$$\log \varphi_{meas}(\lambda, T_{ref}) = \log t_2(\lambda) + \log t_1(\lambda, T_{ref}) \tag{3.3}$$

and so we can eliminate t_2:

$$\log \varphi_{meas}(\lambda, T) - \log \varphi_{meas}(\lambda, T_{ref}) = \log t_1(\lambda, T) - \log t_1(\lambda, T_{ref}) \tag{3.4}$$

Now suppose that we had the same detector (or a detector of identical characteristics) in the flight instrument. From Equation (2.4) we can write, for the 12 micron channel,

$$\log \varphi_{12}(\lambda, T) = \log t_0(\lambda) + \log t_1(\lambda, T)\,. \tag{3.5}$$

Working exactly as before, we can introduce the reference temperature to eliminate the optical transmission function t_0 of the FPA.

$$\log \varphi_{12}(\lambda, T) - \log \varphi(\lambda, T_{ref}) = \log t_1(\lambda, T) - \log t_1(\lambda, T_{ref})\,. \tag{3.6}$$

The right-hand sides of Equations (3.4) and (3.6) are identical, and so

$$\log \varphi_{12}(\lambda, T) - \log \varphi(\lambda, T_{ref}) = \log \varphi_{meas}(\lambda, T) - \log \varphi_{meas}(\lambda, T_{ref})\,. \tag{3.7}$$

Thus, if we have a measurement of the ATSR channel response φ at some reference temperature T_{ref}, we can derive the response at any other detector temperature T.

$$\varphi_{12}(\lambda, T) = \left\{\varphi_{meas}(\lambda, T) \big/ \varphi_{meas}(\lambda, T_{ref})\right\} \varphi_{12}(\lambda, T_{ref}) = f(\lambda, T)\varphi_{12}(\lambda, T_{ref}) \tag{3.8}$$

where the ratio

$$f(\lambda, T) = \varphi_{meas}(\lambda, T) \big/ \varphi_{meas}(\lambda, T_{ref})\,. \tag{3.9}$$

The spectral responses of the ATSR-1 channels at a temperature of 82 K were measured by the UK Met. Office and are tabulated by Mason [**5**]. If therefore we select our reference temperature as 82 K, Equation (3.8) presents the relationship between the baseline ATSR-1 spectral response at 82 K and the corresponding response at any elevated detector temperature T, in terms of the Mullard measurements.

One detail remains. The Mullard measurements do not include measurements at 82 K. We therefore assume that φ_{meas} depends linearly on temperature between 80 and 85 K, and write

$$\varphi_{meas}(\lambda, 82K) = 0.6\varphi_{meas}(\lambda, 80K) + 0.4\varphi_{meas}(\lambda, 85K) \tag{3.10}$$

Our analysis here assumes that the flight detector has identical characteristics to the flight spares measured on the ground. This is not strictly true; different detectors will have different characteristics because of small variations in the alloy composition. The two detectors M03 and M09 differ from each other and will certainly not be identical to the flight detector. However, we can use the ground measurements as a representative set to characterise the likely behaviour of the flight detector, and to estimate the errors that result from operation at elevated detector temperature.

Code to implement this scheme was originally developed by A.M. Zavody in 1996. This code has been corrected and enhanced for the present work and now takes the form of a simple IDL procedure ATSR_SHIFT1. This procedure will calculate a filter profile for the 12 micron channel of ATSR-1 corresponding to an elevated detector temperature T in the range 85 to 110 K. It does this by calculating a correction factor

$f(\lambda, T)$ for the specified temperature, and multiplies the nominal ATSR-1 filter profile by this factor to derive the modified profile corresponding to temperature T.

The correction factor is derived from the measurements made on the flight spare detectors. Three options are provided for the correction factor; it may be derived from the measured profile of detector M03, from the measured profile of M09, or from the mean profile of the two sets of measurements. The last of these options represents Zavody's original implementation; the options of using each set of detector measurements individually were added to allow the differences between the detectors to be investigated.

This procedure has been used to derive modified filter profiles corresponding to the following detector temperatures: 85.0K, 87.5K, 90.0K, 92.5K, 95.0K, 97.5K, 100.0K, 102.5K, 105.0K, 107.5K, and 110.0K. These have been calculated both using the two sets of detector measurements separately, and also using program option 3, to derive the corrected profile from the mean of the two sets of detector measurements according to Zavody's original scheme.

These modified filter profiles may be used to derive modified SST retrieval coefficients for each of the elevated detector temperatures listed, and have also been used in the calculation of the calibration error in Section 4.

Figure 4 illustrates the effect of elevated detector temperature on the 12 micron channel filter profile in a particular case. The figure shows the corrected filter profile for a temperature of 110 K, calculated using the mean of the two detector measurements, superimposed on the nominal filter profile. The profiles are plotted against wave number, and the movement of the low wave number (long-wavelength) edge is clearly shown.

The IDL procedure and filter profiles have been made available to the (A)RC project, to be used in corrected retrieval schemes, and have been used to quantify the effect of elevated detector temperature on the ATSR-1 calibration.

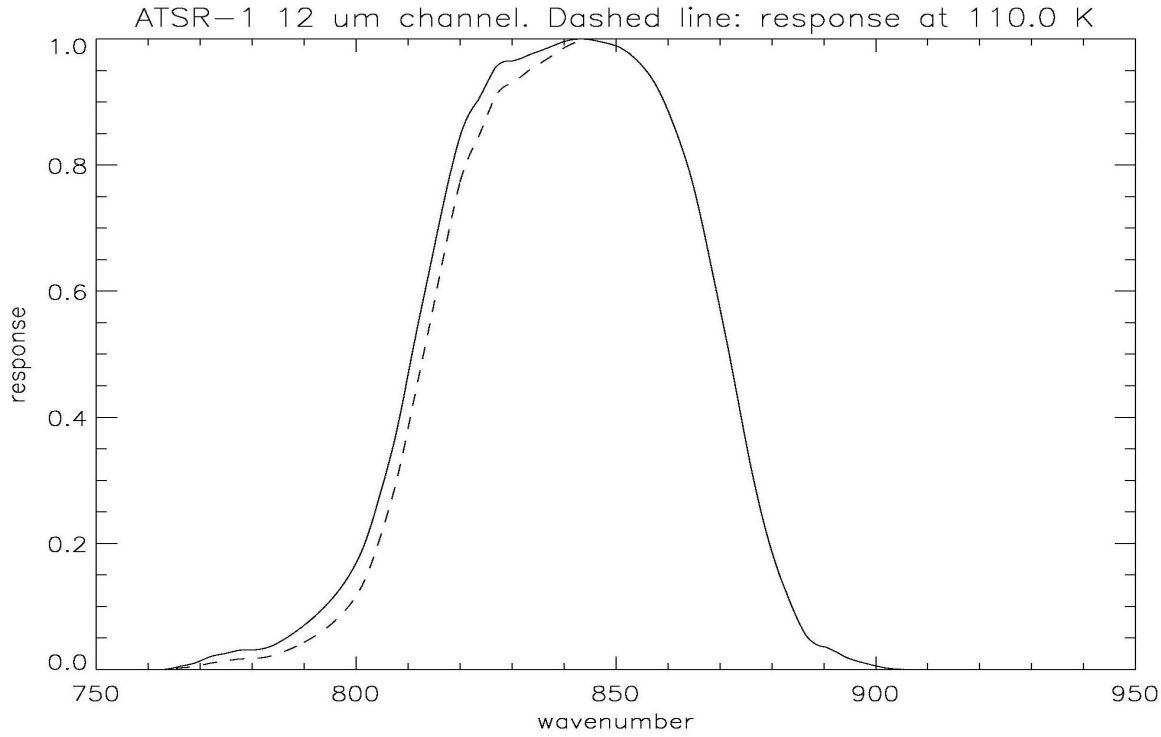

Figure 4: Nominal and corrected profiles for a detector temperature of 110 K.

4 Effect of temperature on ATSR Calibration

4.1 Theoretical Analysis

The calibration of the infra-red channels of ATSR assumes a linear relationship between the radiance incident on the detector and the detector output, and this relationship is determined for each channel separately. (Strictly speaking the ATSR detectors are photon counters, and the detector output is proportional to the number of photons that fall upon it. However, this may be accounted for by a redefinition of response function $\phi_\lambda(\lambda)$, and will be ignored in the following. The detectors also show some non-linearity in practice, but this will not be considered at this stage.)

The radiance incident upon each detector is related to the brightness temperature T by

$$R(T) = \int \phi_\lambda(\lambda) B(\lambda, T) d\lambda \qquad (4.1)$$

where $\phi_\lambda(\lambda)$ is the spectral response of the ATSR channel, expressed as a function of wavelength λ, and $B(\lambda, T)$ is the Planck function. Note that here, following Mason [5] the appearance of λ as a suffix denotes the ATSR-1 channel, and not the independent wavelength variable as elsewhere.

The coefficients of the linear calibration relationship are determined by fixing two measured points, defined by the two calibration black bodies. Let the two black bodies be designated by the indices 1 and 2, and let R_1 and R_2 represent the radiance of black body 1 and 2 respectively. Then the relationship between the radiance R of a pixel and the corresponding detector output C is

$$R = R_1 \frac{C_2 - C}{C_2 - C_1} + R_2 \frac{C - C_1}{C_2 - C_1} \tag{4.2}$$

where C_1 and C_2 are the measured detector outputs (counts) corresponding to the two black bodies.

Equation (4.2) is the essential calibration relationship for ATSR. The quantities C_1 and C_2, are measured directly, while the radiances R_1 and R_2 are derived from the corresponding black body temperatures T_1 and T_2 using

$$R_i = \varepsilon_i R(T_i) + (1 - \varepsilon_i) R(T_b) \tag{4.3}$$

where ε_i is the emissivity of the black body i, i = 1, 2, T_b is the background temperature, and $R(T)$ is the relationship between radiance and temperature for the channel in question.

The brightness temperature of a given pixel is then derived from the calibrated pixel radiance R by inverting the relationship $R(T)$ by means of a look-up table.

Clearly if the spectral response function of the channel depends on the detector temperature, then so does the relationship between radiance and temperature $R(T)$ given by equation (4.1). The use of a temperature-to-radiance relationship corresponding to the wrong detector temperature may therefore give rise to calibration errors. These are likely to be small, because is the calibration ultimately depends upon comparison with physical black bodies of known temperature. Nevertheless, we can quantify the effect as follows.

Suppose that the true relationship between radiance and brightness temperature is $R(T)$ (obtained by evaluating Equation (4.1) with the correct spectral response), but that a relationship $\tilde{R}(T)$, calculated for the detector temperature (in practice 82 K) at which the spectral response was measured, has actually been used for the calibration.

Formally we have

$$R(T) = (1 - w) R_1 + w R_2 \tag{4.4}$$

and

$$\tilde{R}(\tilde{T}) = (1 - w) \tilde{R}_1 + w \tilde{R}_2 , \tag{4.5}$$

where

$$w = (C - C_1)/(C_2 - C_1)$$

and where T, $\tilde{T}$ represent, respectively, the true brightness temperature corresponding to the pixel count C and the erroneous temperature derived from the use of the relationship $\tilde{R}(T)$. Note that w is a measured quantity, but $R(T)$, $\tilde{R}(T)$ represent derived quantities.

In general, there is an error in the radiance corresponding to a pixel count C of

$$dR = (1 - w) dR_1 + w dR_2 \tag{4.6}$$

if

$$\Delta R(T) = R(T) - \tilde{R}(T) \tag{4.7}$$

and dR_1, dR_2 represent $\Delta R(T)$ evaluated at the black body temperatures T_1, T_2, respectively. This is a linear function of C which does not have an extremum in the

range $C_1 \le C \le C_2$, but which satisfies $dR_1 \le dR \le dR_2$ in the same range. However, this quantity does not characterise the error in the calibrated brightness temperature.

If we evaluate Equation (4.7) at $\tilde{T}$, and then expand *R(T)* in a Taylor series about *T*, we get

$$\tilde{R}(\tilde{T}) = R(T) + \frac{dR}{dT}(\tilde{T} - T) - \Delta R(\tilde{T}) \tag{4.8}$$

But (from 4.4 and 4.5)

$$R(T) - \tilde{R}(\tilde{T}) = (1-w)dR_1 + wdR_2 . \tag{4.9}$$

So

$$\frac{dR}{dT}(\tilde{T} - T) = \Delta R(\tilde{T}) - \{(1-w)dR_1 + wdR_2\} \tag{4.10}$$

and the temperature error is approximately

$$T - \tilde{T} = (dR/dT)^{-1}\left\{(1-w)dR_1 + wdR_2 - \Delta R(\tilde{T})\right\} \tag{4.11}$$

This expression depends on the difference between the derived radiance error (Equation 4.6), and the difference function of Equation (4.7), evaluated at $\tilde{T}$. If we ignore emissivity effects, the error is zero at $T = T_1$ or $T = T_2$, which represents the fact that the calibration error is negligible if the pixel radiance is sufficiently close to that of one of the calibration black bodies; that is, if the brightness temperature of the pixel is close to the temperature of the black body.

This algebra is possibly a little opaque, and a diagram may help to explain what it means. In Figure 5 we have sketched the functions $R(T)$ and $\tilde{R}(T)$ as functions of temperature in a section of the interval (T_1, T_2) containing T, $\tilde{T}$. R and $\tilde{R}$ are the corresponding radiance values. The difference between the temperatures T and $\tilde{T}$ is represented by the line segment AB. Now BC = B′C – B′B, while

CB/BA = *dR*/*dT*.

But B′C = $\Delta R(\tilde{T})$ and B′B = $R(T) - \tilde{R}(\tilde{T}) = (1-w)dR_1 + wdR_2$ from (4.9), and so

BA = (CB′ - BB′)/(*dR*/*Dt*)

So

$$T - \tilde{T} = (-\Delta R(\tilde{T}) + (1-w)dR_1 + \mathrm{w}\ dR_2)/(dR/Dt),$$

which is Equation (4.11). Note that the diagram is drawn so that both $\Delta R(\tilde{T})$ and $R(T) - \tilde{R}(\tilde{T})$ are negative quantities, which is correct in practice.

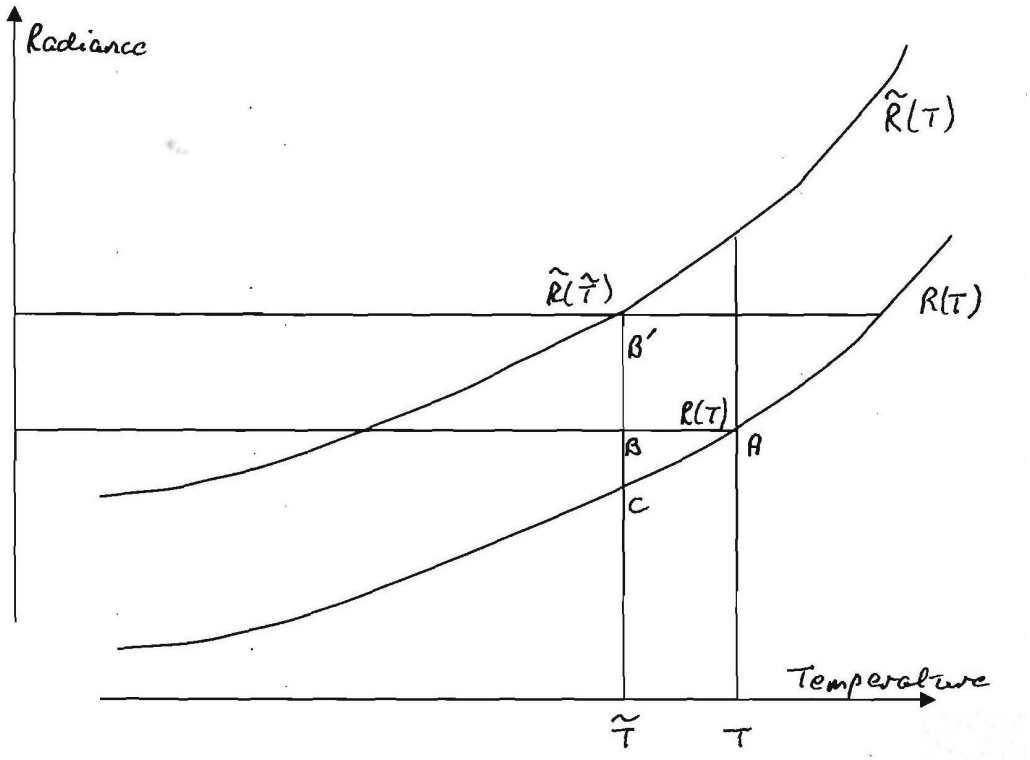

Figure 5: Origin of calibration error.

Loosely we could say that the temperature error is given by the difference between the radiance error and its linear approximation, divided by the slope of the radiance versus temperature curve. However, this might be misleading since the two quantities are evaluated at slightly different temperatures; the radiance error is evaluated at $\tilde{T}$, but the linear approximation is evaluated at the weighted mean temperature

$$T_w = (1-w)T_1 + wT_2 .$$

Note that the result should be independent of arbitrary and independent scale factors applied to R and $\tilde{R}$, since each individual calibration is unchanged if such scale factors are applied. It is not immediately obvious that Equation (4.11) has this property, but we show in the Appendix (Section 8.2) that it does.

This is important because it ensures that we do not need to take a rigorous approach to the normalisation of the channel filter profile $\phi_\lambda(\lambda,T)$ for different detector temperatures. We might expect to normalise this quantity to a maximum value of unity, but this is not necessary. In practice the program (RADACAL) that is used to derive radiance versus temperature tables for use by the radiative transfer model RADGEN, and that was used for the present study, normalises the profiles to constant area, and it is not necessary to change this. The profile area will differ for different detector temperatures, but we can ignore this.

4.2 Numerical results

Code has been written to evaluate Equation 4.11 for any temperature for which a modified filter profile has been derived, and this has been used to characterise the calibration error as a function of detector temperature.

For each detector temperature, a table of radiance versus brightness temperature has been derived by evaluating equation 2.4 using the standard program *RADACAL*. The

calculations were repeated for each of the three filter profile options; those based on detectors M03 and M09, and that based on the mean of the two measurement sets.

An IDL procedure was written to evaluate Equation (4.1) for each detector temperature case at a series of brightness temperatures between 260 K and 300 K, these being the nominal operating temperatures of the calibration black bodies. For each case the maximum calibration error (which occurs close to the centre of the range, ~ 280 K) was extracted.

Figure 6 illustrates the calibration error model for a particular case (a detector temperature of 110 K using the mean filter profile). The radiance error terms from Equation 4.11 are plotted against the calibrated brightness temperature $\tilde{T}$. The lower (concave upwards) curve shows the term $\Delta R(\tilde{T})$, while the upper (concave downwards) curve shows the term $(1-w)dR_1 + wdR_2$. The calibration error is the difference between the two, divided by *dR/dT*. (The dotted line is the straight line between dR_1 and dR_2.)

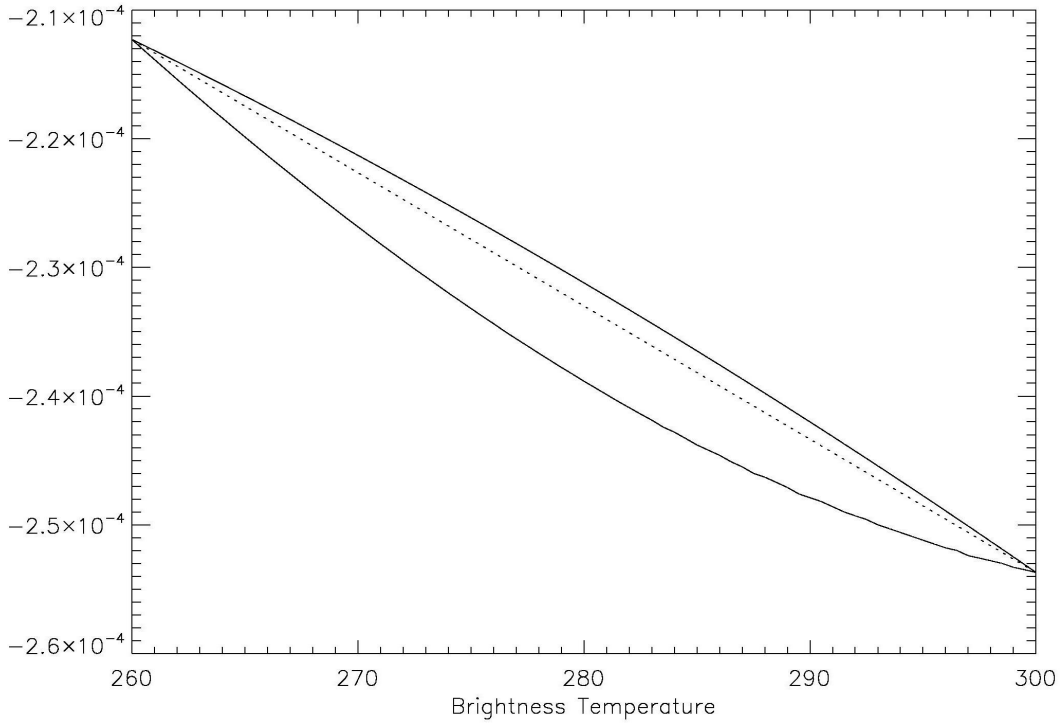

Figure 6: Calibration error terms as a function of brightness temperature for a detector temperature 0f 110 K.

Table 2 below shows the effect of increased detector error on the brightness temperature calibration. The tabulated error is that which results when the response for a detector temperature of 82 K is used to calibrate data measured with the detector temperature shown. The columns headed M03 and M09 give the error calculated from the measurements on the specified detector; the final column shows the error calculated as above using the filter profiles based on the mean of the two measurement sets.

Table 2. Effect of elevated detector temperature on the ATSR-1 calibration.

T_D	Calibration Error (K)		
	Case M03	CaseM09	Combined case
85.0	0.0003	0.0004	0.0003
87.5	0.0005	0.0007	0.0006
90.0	0.0009	0.0010	0.0009
92.5	0.0012	0.0014	0.0013
95.0	0.0016	0.0017	0.0017
97.5	0.0020	0.0020	0.0021
100.0	0.0025	0.0024	0.0026
102.5	0.0030	0.0029	0.0030
105.0	0.0035	0.0035	0.0035
107.5	0.0042	0.0044	0.0043
110.0	0.0049	0.0053	0.0051

Figure 7 shows the maximum calibration error as a function of detector temperature for each of the three cases.

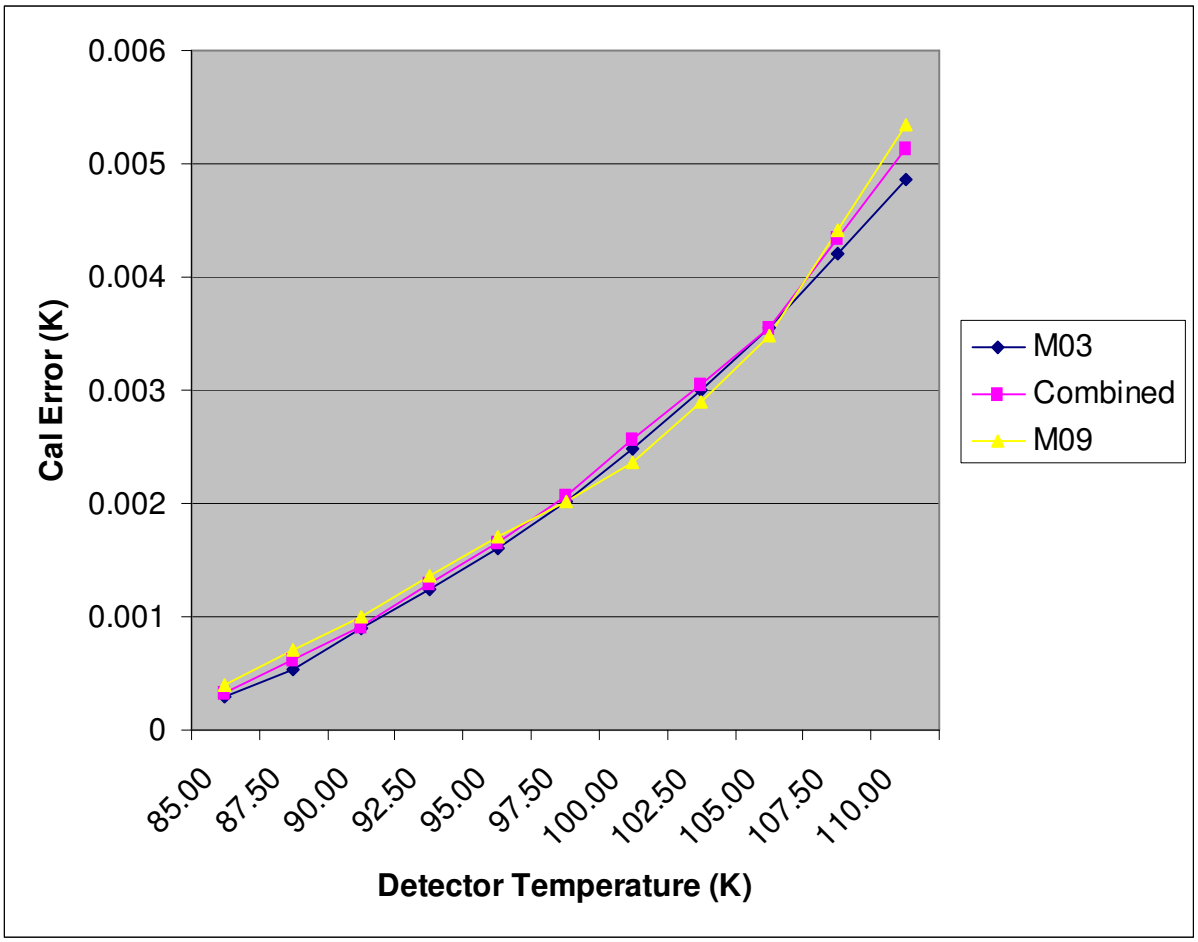

Figure 7: Calibration error versus detector temperature.

We do not have measurements of the flight detector itself, so the applicability of these results depends on the assumption that the flight spares are representative of the in-flight unit. Nevertheless, the good match of the calibration error curves (the maximum difference between the cases M03 and M09 is 0.0005K) for the two detectors separately gives some confidence in this assumption.

If we fit a quadratic function of detector temperature T_D to the combined case data from the final column of Table 2, we find that these data can be represented by the polynomial expression

$$\begin{aligned} dT_m = {} & 4.19228\times10^{-6}(T_D-82.0)^2 \\ & +5.63976\times10^{-5}(T_D-82.0) \\ & +0.0001771 \end{aligned} \tag{4.12}$$

The calibration error model described above is based on the assumptions that the non-zero reflectivity of the black bodies, and any detector non-linearity, can be ignored. These assumptions are discussed in the following sections.

4.3 Effect of Black Body Emissivity

The analysis so far has assumed that the black bodies are ideal, having emissivity of exactly unity. The real calibration black bodies are not quite ideal, and so we should investigate the effect on the calibration errors determined.

As in Section 4.1 above, let ε_1, ε_2 be the emissivities of the black bodies 1 and 2 respectively. From Equation (4.3),

$$R_i = \varepsilon_i R(T_i) + (1-\varepsilon_i)R(T_b), \quad i=1,2 \tag{4.13}$$

represent the black body radiances that should be used in the calibration, while similarly

$$\tilde{R}_i = \varepsilon_i \tilde{R}(T_i) + (1-\varepsilon_i)\tilde{R}(T_b), \quad i=1,2 \tag{4.14}$$

represent the radiances used in the baseline calibration.

The analysis proceeds exactly as in section 4.1 above except that the values of dR_1 and dR_2 in equation (4.11) are derived from the above equations. Thus

$$dR_i = \varepsilon_i \Delta R(T_i) + (1-\varepsilon_i)\Delta R(T_b), \quad i=1,2 \tag{4.15}$$

In particular it is no longer the case that $dR_i = \Delta R(T_i)$, and neither w nor the calibration error vanish at the black body temperatures.

Nevertheless, the effect is small. According to Mason [5], the emissivity values at 12 micron wavelength for the on-board black bodies are $\varepsilon_1 = \varepsilon_2 = 0.9994 \pm 0.0003$.

By adapting the code used to derive the results in Section 4.2 to include the effects of non-ideal emissivity we can quantify the effect. The worst case discrepancy will be obtained by setting $T_b = 0$, granted that this is not physically representative. If this is done, then for a detector temperature of $T_D = 110$ K the following values of w are obtained.

Table 3.

Temperature	w (ε = 0.9994)	w (ε = 1)
260	0.000687	0.0
280	0.457574	0.456612
300	1.00129	1.0

The maximum error calibration error in this case is 0.00520 K as against 0.00513 K, a difference of 0.07 mK. This is clearly negligible. The calibration errors at the black body temperatures are also of the order of 0.07 mK in this case.

4.4 Effect of Detector Non-Linearity

4.4.1 Non-linearity of the ATSR-1 detectors

In the analysis above, we have assumed that the detector output depends linearly on the scene radiance within its operating range. This is not strictly true. Characterisation measurements of the ATSR instrument demonstrated that the 11 and 12 micron channels showed small but detectable non-linearity (Mason, [**5**]).

This non-linearity has been attributed to the effects of Auger recombination in the photoconductive HgCdTe detectors. (Auger recombination refers to non-radiative recombination of electron-hole pairs within the body of the crystal. It is named by analogy with the Auger transitions that are observed within atoms; these are radiationless transitions within atoms that lead, via the ionisation they produce, to the secondary lines observed in X-ray spectroscopy.)

This non-linearity has been characterised empirically in terms of the fractional fall-off, using the following procedure (Mason **[5]**). As part of the ground characterisation of the ATSR-1 instrument, the detector outputs of the 11 and 12 micron channels were measured in an environmental test facility with reference to external black bodies of known temperature and emissivity. The (normalised) detector output was plotted against the calculated radiance of the external targets, and a straight line was fitted to the data points of low radiance. This fitted line was regarded as the ideal detector characteristic, it being assumed that the detector response is linear at low incident radiance. The ratio of the actual detector response to the response predicted by using this fitted line is the 'fractional fall-off' of the detector characteristic, and is a measure of the non-linearity of the response. Formally, let $L_\lambda(T)$ represent the radiation flux incident on the detector. Then for a linear detector, the voltage signal will be proportional to L_λ;

$$\Delta V = \kappa L_\lambda$$

where κ is constant. In the presence of non-linearity, however, κ will be a function of L_λ. The fractional fall-off, then, is the ratio

$$g_\lambda = \kappa(L_\lambda) / \kappa(0) . \qquad (4.15)$$

In order to give an analytic representation of the fractional fall-off, a quadratic function of the normalised source radiance

$$g_\lambda = Z_{0,\lambda} + Z_{1,\lambda}\left(\frac{L_\lambda(T)}{L_\lambda(320k)}\right) + Z_{2,\lambda}\left(\frac{L_\lambda(T)}{L_\lambda(320K)}\right)^2 \qquad (4.16)$$

was fitted to the fractional fall-off data. The radiance was normalised to that at 320 K for the purposes of determining the coefficients. Table 4, from **[5]** gives the numerical values of the coefficients for the 11 and 12 micron channels for ATSR-1.

Table 4: Coefficients for the calculation of fractional fall-off for the 11 and 12 micron channels of ATSR-1

Coeff.	11 micron	12 micron
$Z_{0,\lambda}$	1.00023	1.00085
$Z_{1,\lambda}$	-4.79542e-2	-2.25973e-2
$Z_{2,\lambda}$	-9.54182e-4	-1.54812e-2

It is now a simple matter to apply the non-linearity correction to the look-up table; given the true radiance calculated for the tabular value T, Lλ(T), the fractional fall-off g can be calculated using equation (4.16) above. The corrected radiance for the same tabular temperature is then given by the product

$$g_\lambda L_\lambda(T)\,.$$

4.4.2 Relationship to carrier lifetime

At the root of the physical process is carrier lifetime. When photons fall on the detector, electron-hole pairs are generated. The equilibrium density of excess carriers is

$$\Delta n = \Delta p = \frac{\eta\Phi}{V}\tau\,. \qquad (4.17)$$

In this equation, τ is the carrier lifetime, V is the sample volume, η is the quantum efficiency of the detector, and Φ is the photon flux incident on the detector. Thus the product ηΩ is the number of effective photons falling on the detector per second.

Mason [**5**] gives the following equation for the response of a current-biased detector to incident radiation.

$$\Delta V = \frac{\eta e \mu_e E \Phi}{l} R_d \tau\,. \qquad (4.18)$$

This is equation (9.8) of Mason's thesis; a simple derivation is in the Appendix (Section 8.3). In it, ΔV is the voltage signal from the detector. The symbols η, Φ, and τ are as defined above; the other variables are:

e	The magnitude of the charge on the electron;
μ_e	The carrier mobility of the electron;
E	The electric field in the detector;
l	The length of the detector;
R_d	The resistance of the detector.

Strictly, both R_d and E depend on the photon flux Φ, since R_d refers to the photo-detector itself, while in a current biased system, E must vary as R_d does in order to maintain a constant current. Nevertheless, we assume for the present that the variation of these quantities can be ignored. With this assumption, the relationship between detector output voltage and incident photon flux can be written as

$$\Delta V = K\Phi\tau\,,$$

where K is a constant. This would represent a linear response if the carrier lifetime were constant. In practice however the carrier lifetime τ depends on Δn, which itself depends on Φ. This is the principal source of the non-linearity of the response. Comparing this equation with (4.15) above, we see that the fractional fall-off is given by

$$g_\lambda = \tau(\Phi)/\tau(0)\,. \qquad (4.18)$$

The carrier lifetime also depends on the temperature of the detector. Mason [5] used a physical model of the detector to calculate the sensitivity of the carrier lifetime to changes in the values of the model parameters, and concluded that 'the fall-off in [carrier lifetime] reduces as the detector temperature increases.'

4.4.3 Effect on Calibration Error

We have seen above that the magnitude of the calibration error depends on the curvature of the differential radiance vs. temperature graph. Temperature dependent non-linearity will modify this, and the numerical magnitude of the error should be reassessed. No direct measurements of the dependence of the non-linear detector response on temperature effect are available from which we can do this, and so we must fall back on a physical model.

Mason [5] presented a model from which the carrier lifetime can be estimated. This model has been implemented to try to assess the impact of detector temperature on the non-linearity of the detectors, and hence on the calibration error.

The model, coded in IDL, implements the equations set out by Mason for the case where Auger recombination is the dominant recombination mechanism, and can be used to calculate the carrier lifetime in the HgCdTe detector as a function of incident photon flux and detector temperature. This procedure has been used to derive the fractional fall-off (Equation 4.18) for each of the detector temperatures in Table 2. For each detector temperature the coefficients of a quadratic function, such as those in Equation (4.16), to characterise the dependence of the fractional fall-off on incident flux have been determined.

A modified version of the IDL procedure described in Section 4.2 was written that included the ability to apply fractional fall-off functions, specified in terms of their polynomial coefficients in Equation 4.18, to the radiance vs. brightness temperature functions, and the calculations of Section 4.2 were then repeated, using the modified procedure.

Two sets of calculations were made. In the first, the model non-linearity correction was applied, but the same profile basic profile was used at all detector temperatures. This means that we used

$$R(T) = g_\lambda(T_d)\tilde{R}(T)$$

for all detector temperatures Td. These results show the effect of the non-linearity alone, in the absence of any temperature dependence of the filter profile.

The second set of calculations included both effects as above, using

$$R(T) = g_\lambda L_\lambda(T)$$

in place of

$$R(T) = L_\lambda(T),$$

and with a similar modification applied to the nominal profile $\tilde{R}(T)$. Two sets of calculations were performed, based on the combined response case of Section 4.2. In the first set, the model non-linearity correction was applied, but the same profile basic profile was used at all detector temperatures. This means that we used

$$R(T) = g_\lambda(T_d)\tilde{R}(T)$$

for all detector temperatures Td. These results show the effect of the non-linearity alone, in the absence of any temperature dependence of the filter profile. The second set of calculations included both effects as above. Results are shown in Table 5.

Table 5: Effects of temperature dependent non-linearity on calibration error.

T_D	Calibration Error (K)		
	Filter profile	Non-linearity	Both
85.0	0.0003	0.0003	0.0006
87.5	0.0006	0.0004	0.0010
90.0	0.0009	0.0004	0.0013
92.5	0.0013	0.0005	0.0018
95.0	0.0017	0.0007	0.0024
97.5	0.0021	0.0013	0.0033
100.0	0.0026	0.0021	0.0046
102.5	0.0030	0.0032	0.0063
105.0	0.0035	0.0046	0.0082
107.5	0.0043	0.0063	0.0106
110.0	0.0051	0.0081	0.0132

Results are shown in three columns under the heading ‘Calibration Error’. The first column, headed ‘Filter Profile’, repeats the ‘Combined case’ figures from the final column of Table 2, showing the error without the effects of temperature dependent non-linearity. The second column represents the effects of the non-linearity alone. The final column shows the combined effect of the two. The results are plotted in Figure 8.

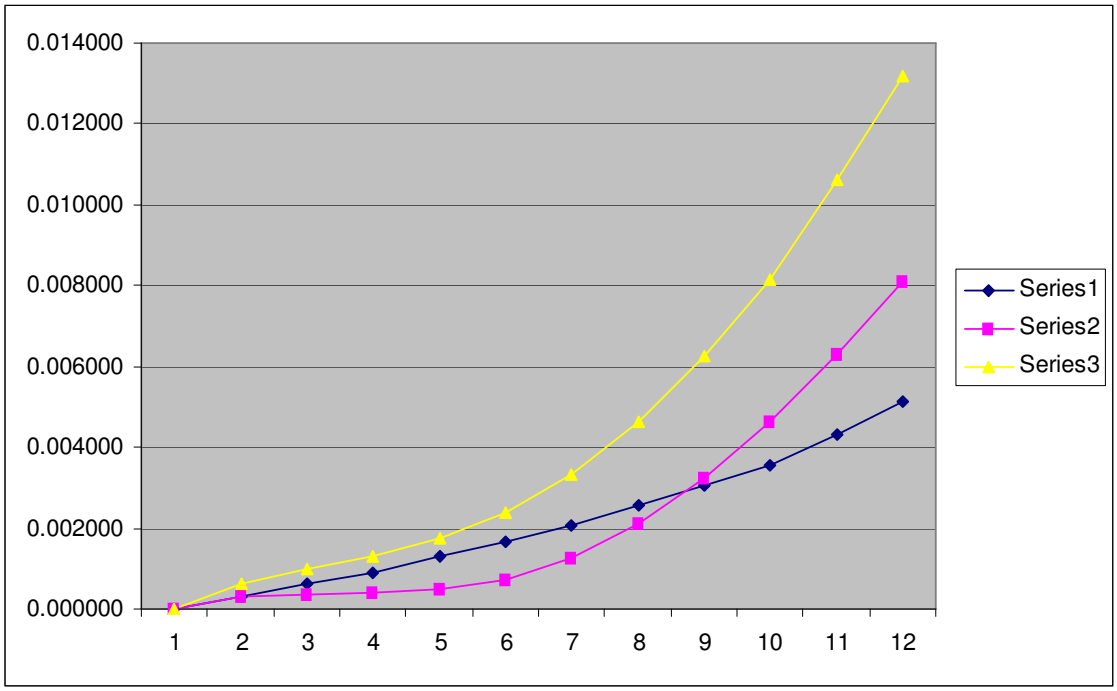

Figure 8: Error based on physical model. Series 1 (Dark Blue): Filter profile effect. Series 2 (Magenta): Modelled Temperature dependent non-linearity. Series 3 (Yellow): Combined effect.

The yellow curve shows the calibration error, calculated from the model, when non-linearity effects are included. It can be seen that the non-linear effects exceed those calculated from the filter profile above about 100 K, and increase to 0.014K at the highest detector temperatures.

It is possible to fit a polynomial function to these data by analogy with Equation 4.12 The result is.

$$\begin{aligned} dT_m &= 2.29718\times10^{-5}(T_D - 82.0)^2 \\ &\quad - 2.27974\times10^{-4}(T_D - 82.0) \\ &\quad + 0.0014229 \end{aligned} \tag{4.19}$$

A number of caveats must be made here.

- Firstly, in the model calculations the value of the incident photon flux $\Phi(T)$ has been taken to correspond to black body radiation of temperature T. This does not take account of any reduced throughput of the actual AATSR optical system. This might have the effect of reducing the range of Φ considered, which in turn would reduce the fractional fall-off at high incident flux.
- The detector model assumes, following Mason, that Auger recombination is the dominant recombination mechanism in the ATSR detectors. Mason based this conclusion at least in part on a paper by Baker et al [**10**], but a careful reading of that paper suggests that it may not be applicable to the ATSR configuration. It is not clear whether or not other mechanisms, in particular Shockley-Read recombination, can be ruled out.

In general, while the results of Section 4.2 relating to the effects of the temperature dependent filter profile and leading to Equation (4.12) are well grounded in the experimental measurements, those of this section are not. The quantitative results are

only as good as the theoretical model, and should be treated with caution pending a more thorough analysis.

5 A Retrospective Calibration Correction

5.1 Outline

If we ignore, for the present, the effects of the temperature dependent non-linearity discussed in Section 4.3, the worst case calibration error is 0.005K. This is less than the 0.01K precision of the gridded product BTs, so is negligible for many applications. Nevertheless, the error is systematic, and may be marginally significant when averaging is used. Averaged BTs are calculated to 0.001 K in routine processing because the coefficient-based retrieval can amplify noise and other random errors. Even in the case of the gridded products, in which the BTs are specified only to a precision of 0.01 K, so that a correction would only modify the rounding error, not to apply it might bias the statistics. It is therefore worthwhile to derive a correction for the effect. If the larger errors resulting from temperature dependent non-linearity are included, this conclusion is reinforced.

To correct the calibration, it is necessary to know the black body temperatures used to calibrate the data in order to recover the black body radiances. The procedure is first to recover $\tilde{R}$ from the brightness temperature. It is then necessary to know the black body radiances to recover w (via Equation 4.5) to permit a corrected calibration to be derived.

Thus it is not possible to generate a simple look-up table that gives the calibration correction as a function (say) of the detector temperature. For each detector temperature the calibration correction depends on the two black body temperatures as well as on the brightness temperature itself, and a look-up table would need to consist of a 3-dimensional matrix. However, we can instead derive a simple analytic model, which should be simple and inexpensive to apply. In outline, the procedure is as follows.

Inspection of Figure 6 suggests that, to a good approximation, the error function for a given detector temperature is a quadratic function of brightness temperature that is zero at the black body temperatures T_1 and T_2. It will therefore have the form

$$a(T_2 - \tilde{T})(\tilde{T} - T_1),$$

and we assume that a is constant, as a function of the black body temperatures T_1 and T_2 as well as of $\tilde{T}$; this will be justified later. For given values of T_1, T_2 this expression has a maximum at $\tilde{T} = (T_2 + T_1)/2$ equal to $a(T_2 - T_1)^2/4$. It follows that we can write the calibration error as

$$T - \tilde{T} = (dR/dT)^{-1}\{a(T_2 - \tilde{T})(\tilde{T} - T_1)\}. \qquad (5.1)$$

We have modelled the maximum value of the calibration correction for particular values of the black body temperatures $T_1 = T_1^m$, $T_2 = T_2^m$. If the corresponding maximum is dT_m, then

$$dT_m = (dR/dT)^{-1}\{a(T_1^m - T_2^m)^2/4\}$$

Thus $a(dR/dT)^{-1} = 4dT_m/(T_1^m - T_2^m)^2$,

and

$$T - \tilde{T} = 4dT_m \frac{(T_2 - \tilde{T})(\tilde{T} - T_1)}{(T_1^m - T_2^m)^2} \tag{5.2}$$

The maximum temperature errors for the case $T_1^m = 260$, $T_2^m = 300$K (again discounting the effects of temperature depemdent non-linearity) are given in Table 2. By fitting a quadratic function of detector temperature T_D to the combined case data from the final column, we found that these data can be represented by Equation (4.12), repeated here for reference:

$$\begin{aligned} dT_m = {} & 4.19228\times10^{-6}(T_D - 82.0)^2 \\ & + 5.63976\times10^{-5}(T_D - 82.0) \\ & + 0.0001771 \end{aligned}$$

Equating these two expressions for dT_m, we can deduce that

$$T - \tilde{T} = \left\{ \begin{matrix} (4.19228\times10^{-6}(T_D - 82)^2 + \\ 5.63976\times10^{-5}(T_D - 82) + 0.0001771) \end{matrix} \middle/ 400 \right\} (T_2 - \tilde{T})(\tilde{T} - T_1) \tag{5.3}$$

and this expression represents the calibration error as a function of the detector temperature T_D and the black body temperatures T_1 and T_2.

Strictly this formula is not quite accurate, because we have in effect assumed that the derivative term is constant. In fact it is not; if the second derivative is constant, then the first varies approximately linearly across the range. The variation is

$$\left.\frac{dR}{dT}\right|_T = \left.\frac{dR}{dT}\right|_{T=280} (1 + 0.008607(T - 280)) \tag{5.4}$$

and we should apply this correction factor to the above equation. If this is done we obtain the full correction

$$\begin{aligned} T - \tilde{T} = {} & \left\{(4.19228\times10^{-6}(T_D - 82)^2 + 5.63976\times10^{-5}(T_D - 82) + 0.0001771)/400\right\}\times \\ & (1 + 0.008607(\tilde{T} - 280.0))(T_2 - \tilde{T})(\tilde{T} - T_1) \end{aligned} \tag{5.5}$$

Equation (4.19) was derived for a detector temperature of 110K. Strictly the relationship depends on the detector temperature. However, in practice the curves scale sufficiently closely that this complication can be ignored.

The full correction is therefore represented by Equation (5.5), while the simplified correction is represented by Equation (5.3). Either equation can be evaluated as a function of the detector temperature T_D and the black body temperatures T_1 and T_2. These are available in the telemetry.

In order to account for the effects of temperature dependent non-linearity, we can re-evaluate Equation 5.3 but substituting the polynomial of Equation (4.19) for that of Equation (4.12). The result is

$$T - \tilde{T} = \left\{ \begin{matrix} (2.29718\times10^{-5}(T_D - 82)^2 - \\ 2.27974\times10^{-4}(T_D - 82) + 0.0014229) \end{matrix} \middle/ 400 \right\} (T_2 - \tilde{T})(\tilde{T} - T_1) \tag{5.6}$$

5.2 Formal derivation

Our argument leading to Equation (4.13) was not rigorous. To demonstrate this correction more formally, we proceed as follows.

Expand the radiance to brightness functions as Taylor series about the cold black body temperature T_1.

$$R(T) = R(T_1) + \left.\frac{dR}{dT}\right|_{T_1}(T-T_1) + \tfrac{1}{2}\left.\frac{d^2R}{dT^2}\right|_{T_1}(T-T_1)^2 + \tfrac{1}{6}\left.\frac{d^3R}{dT^3}\right|_{T_1}(T-T_1)^3 + \ldots \quad (5.7)$$

$$\tilde{R}(T) = \tilde{R}(T_1) + \left.\frac{d\tilde{R}}{dT}\right|_{T_1}(T-T_1) + \tfrac{1}{2}\left.\frac{d^2\tilde{R}}{dT^2}\right|_{T_1}(T-T_1)^2 + \tfrac{1}{6}\left.\frac{d^3\tilde{R}}{dT^3}\right|_{T_1}(T-T_1)^3 + \ldots \quad (5.8)$$

It follows immediately that

$$\Delta R(T) = \Delta R(T_1) + \left.\frac{d\Delta R}{dT}\right|_{T_1}(T-T_1) + \tfrac{1}{2}\left.\frac{d^2\Delta R}{dT^2}\right|_{T_1}(T-T_1)^2 + \tfrac{1}{6}\left.\frac{d^3\Delta R}{dT^3}\right|_{T_1}(T-T_1)^3 + \ldots \quad (5.9)$$

where

$$\Delta R(T) = R(T) - \tilde{R}(T)$$

and

$$\frac{d^n\Delta R}{dT^n} = \frac{d^nR}{dT^n} - \frac{d^n\tilde{R}}{dT^n}$$

for all n. We can also express the weight w in terms of T as follows.

$$w = \frac{\tilde{R}(\tilde{T}) - \tilde{R}_1}{\tilde{R}_2 - \tilde{R}_1} \quad (5.10)$$

Thus adopting the abbreviated notation $R^{(n)} = dR^n/dT^n$

$$\begin{aligned} w &= \frac{\tilde{R}^{(1)}(\tilde{T}-T_1) + \tfrac{1}{2}\tilde{R}^{(2)}(\tilde{T}-T_1)^2 + \tfrac{1}{6}\tilde{R}^{(3)}(\tilde{T}-T_1)^3 + \ldots}{\tilde{R}^{(1)}(T_2-T_1) + \tfrac{1}{2}\tilde{R}^{(2)}(T_2-T_1)^2 + \tfrac{1}{6}\tilde{R}^{(3)}(T_2-T_1)^3 + \ldots} \\ &= \frac{\tilde{T}-T_1}{T_2-T_1}\left\{\frac{\tilde{R}^{(1)} + \tfrac{1}{2}\tilde{R}^{(2)}(\tilde{T}-T) + \tfrac{1}{6}\tilde{R}^{(3)}(\tilde{T}-T)^2 + \ldots}{\tilde{R}^{(1)} + \tfrac{1}{2}\tilde{R}^{(2)}(T_2-T_1) + \tfrac{1}{6}\tilde{R}^{(3)}(T_2-T_1)^2 + \ldots}\right\} \\ &= \frac{\tilde{T}-T_1}{T_2-T_1}\{1-\delta\} \end{aligned} \quad (5.11)$$

where

$$\delta = \frac{\tfrac{1}{2}\tilde{R}^{(2)}(T_2-\tilde{T}) + \tfrac{1}{6}\tilde{R}^{(3)}\left[(T_2-T_1)^2 - (\tilde{T}-T_1)^2\right] + \ldots}{\tilde{R}^{(1)} + \tfrac{1}{2}\tilde{R}^{(2)}(T_2-T_1) + \tfrac{1}{6}\tilde{R}^{(3)}(T_2-T_1)^2 + \ldots} \quad (5.11a)$$

Note that the term of order n in the numerator of this expression has the general form

$$\frac{1}{n!}\tilde{R}^{(n)}\left[(T_2-T_1)^n - (\tilde{T}-T_1)^n\right] = \frac{1}{n!}\tilde{R}^{(n)}\left[(T_2-\tilde{T})\sum_{p=0}^{n-1}(T_2-T_1)^{n-1-p}(\tilde{T}-T_1)^p\right],$$

where we have used the general result that

$$a^n - b^n = (a-b)(a^{n-1} + a^{n-2}b + a^{n-3}b^2 + \ldots + b^{n-1})$$

Consider the term within brackets { } in equation (4.11). This can be written as

$$dR_1 + (dR_2 - dR_1)\left(\frac{\tilde{T} - T_1}{T_2 - T_1}\right)(1-\delta) - \Delta R(\tilde{T}) \tag{5.12}$$

$$= \quad dR_1 + (dR_2 - dR_1)\left(\frac{\tilde{T} - T_1}{T_2 - T_1}\right) - \Delta R(\tilde{T}) \tag{5.12a}$$

$$-(dR_2 - dR_1)\left(\frac{\tilde{T} - T_1}{T_2 - T_1}\right)\delta \tag{5.12b}$$

The expression (5.12a) can be written

$$dR_1 + \left(\frac{\tilde{T} - T_1}{T_2 - T_1}\right)\left(\left.\frac{d\Delta R}{dT}\right|_{T_1}(T_2 - T_1) + \tfrac{1}{2}\left.\frac{d^2\Delta R}{dT^2}\right|_{T_1}(T_2 - T_1)^2 + \tfrac{1}{6}\left.\frac{d^3\Delta R}{dT^3}\right|_{T_1}(T_2 - T_1)^3 + \ldots\right)$$

$$-\left(dR_1 + \left.\frac{d\Delta R}{dT}\right|_{T_1}(\tilde{T} - T_1) + \tfrac{1}{2}\left.\frac{d^2\Delta R}{dT^2}\right|_{T_1}(\tilde{T} - T_1)^2 + \tfrac{1}{6}\left.\frac{d^3\Delta R}{dT^3}\right|_{T_1}(\tilde{T} - T_1)^3 + \ldots\right)$$

$$= \tfrac{1}{2}\left.\frac{d^2\Delta R}{dT^2}\right|_{T_1}(\tilde{T} - T_1)(T_2 - \tilde{T}) + \tfrac{1}{6}\left.\frac{d^3\Delta R}{dT^3}\right|_{T_1}(\tilde{T} - T_1)\left[(T_2 - T_1)^2 - (\tilde{T} - T_1)^2\right] + \ldots$$

The general term in this expression is

$$\frac{1}{n!}\Delta R^{(n)}(\tilde{T} - T_1)\left[(T_2 - T_1)^{n-1} - (\tilde{T} - T_1)^{n-1}\right] = \frac{1}{n!}\Delta R^{(n)}\left[(\tilde{T} - T_1)(T_2 - \tilde{T})\sum_{p=0}^{n-2}(T_2 - T_1)^{n-2-p}(\tilde{T} - T_1)^p\right]$$

for n ≥ 2. Each term includes a factor $(\tilde{T} - T_1)(T_2 - \tilde{T})$, so that each separately vanishes when $\tilde{T} = T_1$ and $\tilde{T} = T_2$. Thus the whole expression vanishes at the black body temperatures, as it should.

The expression (5.12b) including δ can be written as

$$-(dR_2 - dR_1)\left(\frac{\tilde{T} - T_1}{T_2 - T_1}\right)\delta$$

$$= -(dR_2 - dR_1)\left(\frac{\tilde{T} - T_1}{\tilde{R}_2 - \tilde{R}_1}\right)\left(\tfrac{1}{2}\tilde{R}^{(2)}(T_2 - \tilde{T}) + \tfrac{1}{6}\tilde{R}^{(3)}\left[(T_2 - T_1)^2 - (\tilde{T} - T_1)^2\right] + \ldots\right)$$

where again the general term in the final parentheses can be written as above, so that each term includes a factor $(\tilde{T} - T_1)(T_2 - \tilde{T})$, and separately vanishes when $\tilde{T} = T_1$ and when $\tilde{T} = T_2$. Note that we have made use of the fact that the denominator in the expression (5.11a) is equivalent to $(\tilde{R}_2 - \tilde{R}_1)/(T_2 - T_1)$.

So far we have retained the full series expansions for each term. However, it is reasonable to assume, and will be justified below, that over the relevant range of temperatures we can neglect terms involving third and higher derivatives, and retain only the second derivative terms. In this case the expression (5.12) becomes

$$\left\{ \tfrac{1}{2}\left.\frac{d^2\Delta R}{dT^2}\right|_{T_1} - \tfrac{1}{2}\left(\frac{dR_2 - dR_1}{\tilde{R}_2 - \tilde{R}_1}\right)\left.\frac{d^2\tilde{R}}{dT^2}\right|_{T_1} \right\}(T_2 - \tilde{T})(\tilde{T} - T_1) \qquad (5.13)$$

For given values of the black body temperatures T_1 and T_2, the expression in parentheses is constant. The second derivatives appearing in this expression are constants as functions of T_2 and $\tilde{T}$, both evaluated at $T = T_1$. Moreover to the extent that higher order derivatives are negligible the second derivatives will be independent of T_1. The quantity

$$\left(\frac{dR_2 - dR_1}{\tilde{R}_2 - \tilde{R}_1}\right)$$

is not strictly constant when T_1 and T_2 are varied. However, if $(dR_2 - dR_1)$ is plotted against $(\tilde{R}_2 - \tilde{R}_1)$ for a range of values of T_1 and T_2, a linear correlation is seen, with approximate slope 6.67×10^{-4}, so we can assume that their ratio is constant to a sufficiently good approximation. With these assumptions therefore, the coefficient in parentheses { } in (5.13) can be regarded as constant, justifying our assumption that a is constant in Equation (5.1).

5.3 Justification of Approximations

We assumed above that derivatives of higher order than the second in the series expansions can be ignored. Consider first the function $\tilde{R}$.

$\tilde{R}$ is a monotonically increasing function of T that curves upward. That is to say, it has a positive slope and a positive second derivative throughout the range of interest.

We can use the radiance functions on which the calculations [above] are based to quantify these. By numerical differentiation we can estimate the derivatives at the nominal black body temperatures as follows, when T_D = 110 K, as follows (Table 6).

Table 6.

	T_1 = 260 K	T_2 = 300 K
dR/dT	0.00123073	0.00174691
d^2R/dT^2	1.29566E-5	1.25915E-5

It is not possible to estimate the third derivative using numerical differentiation, because the rounding errors in the single precision data are too great. However we can estimate the third derivative by fitting a second order polynomial to the first derivative data and differentiating that. By this means we can estimate

$$d^3R/dT^3 = -7.71 \times 10^{-9}.$$

From Table 6 the approximate order of magnitude of d^2R/dT^2 here is 1.3×10^{-5} and the ratio of the derivatives is therefore of the order of 6×10^{-4}, which seems adequately negligible.

The case of the derivatives of ΔR is slightly more complex. Because this is a difference of two radiance versus temperature function, the relative numerical precision of the single precision values is lower, and it is only possible to derive the first derivatives by numerical differentiation. For T_D = 110 K the values are (Table 7):

Table 7.

	T_1 = 260 K	T_2 = 300 K
dR/dT	-1.572 E-6	-4.023 E-7

The slope increases algebraically from T_1 to T_2. From the above we can estimate the second derivative in the range to be 2.92×10^{-8}. We can also estimate the third derivative as before by fitting a quadratic function to the dR/dT data. The result is

$$d^3R/dT^3 = 3.31 \times 10^{-10}.$$

The ratio of the third to the second derivative is then of the order of 0.011. Although small, this is not quite negligible, since the second and third order terms in the expansion of ΔR are in the ratio

$$\tfrac{1}{2}\Delta R^{(2)} : \tfrac{1}{6}\Delta R^{(3)}(T_2 - 2T_1 + \tilde{T}).$$

Evaluated at the mid-range $\tilde{T} = (T_2 + T_1)/2$ this is

$$\tfrac{1}{2}\Delta R^{(2)} : \tfrac{1}{4}\Delta R^{(3)}(T_2 - T_1)$$

and because $(T_2 - T_1)$ is large (40 K) is of the order of 4.4 **:** 1.

At this point we must recognise that in cases where the higher derivatives are significant, the expression (5.13) is still valid provided the coefficient is evaluated at the centre of the range, where the calibration error is greatest.

If the third derivative term in the expansion of ΔR is retained, expression (5.13) becomes

$$\left\{ \tfrac{1}{2}\left.\frac{d^2\Delta R}{dT^2}\right|_{T_1} + \tfrac{1}{6}\left.\frac{d^3\Delta R}{dT^3}\right|_{T_1}(T_2 - 2T_1 + \tilde{T}) - \tfrac{1}{2}\left(\frac{dR_2 - dR_1}{\tilde{R}_2 - \tilde{R}_1}\right)\left.\frac{d^2\tilde{R}}{dT^2}\right|_{T_1} \right\}(T_2 - \tilde{T})(\tilde{T} - T_1)$$

Evaluated at mid-range this becomes

$$\left\{ \tfrac{1}{2}\left.\frac{d^2\Delta R}{dT^2}\right|_{T_1} + \tfrac{1}{6}\left.\frac{d^3\Delta R}{dT^3}\right|_{T_1}(\tfrac{3}{2}(T_2 - T_1)) - \tfrac{1}{2}\left(\frac{dR_2 - dR_1}{\tilde{R}_2 - \tilde{R}_1}\right)\left.\frac{d^2\tilde{R}}{dT^2}\right|_{T_1} \right\}(T_2 - \tilde{T})(\tilde{T} - T_1)$$

in which the term in brackets { } can be regarded as constant as before. Note that to this level of approximation,

$$\left.\frac{d^2\Delta R}{dT^2}\right|_{T_1} + \left.\frac{d^3\Delta R}{dT^3}\right|_{T_1}\frac{(T_2 - T_1)}{2} = \left.\frac{d^2\Delta R}{dT^2}\right|_{(T_1+T_2)/2}$$

which we can represent by the shorthand $\Delta R^{(2)}_{1.5}$.

The difference between these two expressions, which has a cubic dependence on $\tilde{T}$, is

$$\left\{ \tfrac{1}{6}\left.\frac{d^3\Delta R}{dT^3}\right|_{T_1}(\tilde{T} - \tfrac{1}{2}(T_2 + T_1)) \right\}(T_2 - \tilde{T})(\tilde{T} - T_1) \qquad (5.14)$$

It is straightforward to show that this error term has extrema at

$$\tilde{T} = \tfrac{1}{2}(T_2 + T_1) \pm \tfrac{1}{2\sqrt{3}}(T_2 - T_1),$$

and at these points the second and third derivative terms are now in the ratio

$$\tfrac{1}{2}\Delta R^{(2)}_{1.5} : \tfrac{1}{6}\Delta R^{(3)}(\tfrac{1}{2\sqrt{3}}(T_2 - T_1))$$

which evaluates to 23.6 : 1, a much more satisfactory value.

An alternative derivation, which will be of particular interest to keen algebraists and enthusiasts for the Taylor series, will be found in the Appendix (Section 8.1).

6 Summary

The variation in the ATSR-1 12 micron channel filter profile with detector temperature has been characterised on the basis of measurements of the flight spare detectors. Modified filter profiles can be calculated for any detector temperature in the range 85 to 110 K, for use in SST retrieval.

The calibration error has been modelled as a function of detector temperature, and a simple calibration correction algorithm has been devised that can be applied to brightness temperature values in the Level 1B products from ATSR-1 to correct for the use of the baseline brightness temperature to radiance relationship in routine processing.

However, temperature dependent non-linearity will increase the calibration error above that due to the profile effect alone. An attempt has been made to quantify this, based on a theoretical model of the carrier lifetime, and a tentative correction has been presented. However, there may be some doubt as to the validity of Mason's [**5**] conclusion, that Auger recombination sufficiently explains the observed detector non-linearity, while experimental measurements in support of the physical model are not available. This correction should therefore be treated with caution pending a more thorough analysis.

7 References

[1] Murray, M.J., Allen, M.R., Mutlow, C.T., and Zavody, A. 'Actual and potential information in dual-view radiometric observations of sea surface temperature from ATSR.' J.G.R. 103 (C4), 8153 -8165, 1998.

[2] Birks, A.R. The Impact of 12 micron Detector temperature on ATSR-1 Data Processing. Presented at the International Workshop on the Applications of the ERS Along track Scanning radiometer, ESRIN, Frascati, 23 – 25 June 1999.

[3] Norton, P. 'HgCdTe infrared detectors', Opto-electronics Review, **10**, 159 – 174, 2002.

[4] Kruse, P.W. 'The emergence of $Hg_{1-x}Cd_xTe$ as a modern infra-red sensitive material', in *Semiconductors and Semimetals, Volume 18: Mercury Cadmium Telluride*, edited by R.K. Willardson and A.C.Beer, London, Academic Press, 1981.

[5] Mason, G. ATSR Test and Calibration Report, Document Reference ER-RP-OXF-AT-0001.Oxford University, September 1991.

[6] Hansen, G.L., Schmit, J.L., and Casselman, T.N., Energy gap versus alloy composition and temperature in $Hg_{1-x}Cd_xTe$, J. Appl. Phys. **53**, 7099 - 7101, 1982.

[7] Topics in Applied Physics, **19**, Ed. R.J Keyes.

[8] Edwards, T. et al, The Along-Track Scanning Radiometer - measurement of sea-surface temperature from ERS-1. *Journal of the British Interplanetary Society,* **43**, 160 - 180, 1990.

[9] Zavody, A.M., C.T. Mutlow and D.T. Llewellyn-Jones. 'A radiative transfer model for sea-surface temperature retrieval for the Along-Track Scanning Radiometer.' Journal of Geophysical Research, **100** (C1), 937 - 952, 1995.

[10] Baker, I.M., Capocci, F.A., Charlton, D.E., and Wotherspoon, J.T.M. Recombination in Cadmium Mercury Telluride Photodetectors. Solid State Electronics, **21**, 1475 – 1480, 1978.

8 Appendix

8.1 Alternative Form of the Series Expansion

There is actually a more direct, albeit more laborious way to demonstrate the result of Section 5.3. This is to expand the various functions not about T_1 but about some fixed temperature T_0 in the range $T_1 < T_0 < T_2$. If this is done, it is found that the second derivative term has essentially the same form as before, but the coefficients of the third and higher derivatives become more complex.

We introduce the notation

$$S^{(m)}(T,T_1)=\sum_{p=0}^{m}(T-T_0)^{m-p}(T_1-T_0)^p\ .$$

Since we are treating T_0 as a constant, we leave the dependence of this expression on T_0 implicit.

Proceeding as before, we can show that the expression (5.12a) becomes

$$\tfrac{1}{2}\frac{d^2\Delta R}{dT^2}\bigg|_{T_0}(\tilde{T}-T_1)\left[S^{(1)}(T_2,T_1)-S^{(1)}(\tilde{T},T_1)\right]+\tfrac{1}{6}\frac{d^3\Delta R}{dT^3}\bigg|_{T_0}(\tilde{T}-T_1)\left[S^{(2)}(T_2,T_1)-S^{(2)}(\tilde{T},T_1)\right]+\ldots$$

Clearly the general term has the form

$$\frac{1}{n!}\Delta R^{(n)}(\tilde{T}-T_1)\left[S^{(n-1)}(T_2,T_1)-S^{(n-1)}(\tilde{T},T_1)\right].$$

Now

$$\left[S^{(1)}(T_2,T_1)-S^{(1)}(\tilde{T},T_1)\right]=T_2-\tilde{T}$$

and in general

$$\begin{aligned}\left[S^{(m)}(T_2,T_1)-S^{(m)}(\tilde{T},T_1)\right]&=\sum_{p=0}^{m}(T_2-T_0)^{m-p}(T_1-T_0)^p-\sum_{p=0}^{m}(\tilde{T}-T_0)^{m-p}(T_1-T_0)^p\\&=\sum_{p=0}^{m-1}(T_1-T_0)^p\left[(T_2-T_0)^{m-p}-(\tilde{T}-T_0)^{m-p}\right]\\&=(T_2-\tilde{T})\sum_{p=0}^{m-1}(T_1-T_0)^p\sum_{q=0}^{m-1-p}(T_2-T_0)^{m-1-p-q}(\tilde{T}-T_0)^q\end{aligned}$$

Note that the terms for $p = m$ in the original sums always cancel. Again each term has a factor $(T_2-\tilde{T})$.

Similarly we find that

$$\delta=\frac{\tfrac{1}{2}\tilde{R}^{(2)}(T_2-\tilde{T})+\tfrac{1}{6}\tilde{R}^{(3)}\left[S^{(2)}(T_2,T_1)-S^{(2)}(\tilde{T},T_1)\right]+\ldots}{\tilde{R}^{(1)}+\tfrac{1}{2}\tilde{R}^{(2)}S^{1}(T_2,T_1)+\tfrac{1}{6}\tilde{R}^{(3)}S^{(2)}(T_2,T_1)+\ldots},$$

and the δ term (5.12b) becomes

$$-(dR_2-dR_1)\left(\frac{\tilde{T}-T_1}{\tilde{R}_2-\tilde{R}_1}\right)\left(\tfrac{1}{2}\tilde{R}^{(2)}(T_2-\tilde{T})+\tfrac{1}{6}\tilde{R}^{(3)}\left[S^{(2)}(T_2,T_1)-S^{(2)}(\tilde{T},T_1)\right]+\ldots\right)$$

Ignoring the third and higher derivatives the complete expression (5.12) now becomes

$$\left\{ \tfrac{1}{2}\left.\frac{d^2\Delta R}{dT^2}\right|_{T_0} - \tfrac{1}{2}\left(\frac{dR_2 - dR_1}{\tilde{R}_2 - \tilde{R}_1}\right)\left.\frac{d^2\tilde{R}}{dT^2}\right|_{T_0} \right\}(T_2 - \tilde{T})(\tilde{T} - T_1)$$

which has the identical form to (5.13) except that the derivatives are evaluated at T_0 rather than at T_1. The second derivatives are independent of both T_1 and T_2, and so with the same proviso as before the coefficient term in brackets { } can be regarded as constant. Moreover the leading error term is

$$\tfrac{1}{6}\left.\frac{d^3\Delta R}{dT^3}\right|_{T_0} (T_2 - \tilde{T})(\tilde{T} - T_1)[\tilde{T} - \tfrac{1}{2}(T_2 + T_1) - 3(T_0 - \tfrac{1}{2}(T_2 + T_1))]$$

which reduces to (5.14) when $T_1 + T_2 = 2T_0$, justifying the latter.

8.2 Scale Invariance

In Section 4.1 we stated that the calibration error dT is essentially invariant with respect to scale factors applied to the radiance versus temperature functions. Here we demonstrate this. As before let us adopt the abbreviated notation

$$R_1^{(2)} = \left.\frac{d^2R}{dT^2}\right|_{T_1}, \quad \tilde{R}_1^{(2)} = \left.\frac{d^2\tilde{R}}{dT^2}\right|_{T_1}.$$

Then the expression (5.13) can be written

$$\tfrac{1}{2}\left[(R_1^{(2)} - \tilde{R}_1^{(2)})(\tilde{R}_2 - \tilde{R}_1) - \tilde{R}_1^{(2)}(R_2 - \tilde{R}_2 - R_1 + \tilde{R}_1)\right](\tilde{T} - T_1)(T_2 - \tilde{T})/(\tilde{R}_2 - \tilde{R}_1)$$

The expression in square brackets expands to

$$\begin{aligned}&\left[R_1^{(2)}\tilde{R}_2 - R_1^{(2)}\tilde{R}_1 - \tilde{R}_1^{(2)}\tilde{R}_2 + \tilde{R}_1^{(2)}\tilde{R}_1 - \tilde{R}_1^{(2)}R_2 + \tilde{R}_1^{(2)}\tilde{R}_2 + \tilde{R}_1^{(2)}R_1 - \tilde{R}_1^{(2)}\tilde{R}_1\right] \\ &= \left[R_1^{(2)}\tilde{R}_2 - R_1^{(2)}\tilde{R}_1 - \tilde{R}_1^{(2)}R_2 + \tilde{R}_1^{(2)}R_1\right]\end{aligned}$$

Each term in the final expression is the product of a term linear in R, and one linear in $\tilde{R}$. Substituting in (4.11), we find that the expression for the calibration error becomes

$$T - \tilde{T} = \left(\frac{dR}{dT}\right)^{-1}\left\{\tfrac{1}{2}\left[R_1^{(2)}\tilde{R}_2 - R_1^{(2)}\tilde{R}_1 - \tilde{R}_1^{(2)}R_2 + \tilde{R}_1^{(2)}R_1\right]\frac{(\tilde{T} - T_1)(T_2 - \tilde{T})}{(\tilde{R}_2 - \tilde{R}_1)}\right\}$$

If we substitute aR for R and $b\tilde{R}$ for $\tilde{R}$ in this formula, we find that the scale factors a and b cancel, and the formula is invariant with respect to them.

Although we have only demonstrated this in the case of the second order approximation, the result is in fact exact. We can take each higher derivative term and show, by exactly the same algebra, that it is invariant in respect to an arbitrary scale factor applied to either R or $\tilde{R}$, and hence that the sum as a whole is also.

8.3 Detector response

In this section we provide a simple derivation of the Equation for detector response given in Section 4.3.

Let μe and μh be the carrier mobilities for electrons and holes respectively. Then by definition the drift velocities of the two kinds of carrier in a uniform electric field E are $\mu_e E$ and $\mu_h E$ respectively.

It follows that, under the influence of an applied field E, the charge per second crossing a surface of area A orthogonal to the field is

$$I = (n\mu_e + p\mu_h)eEA\,, \tag{8.3.1}$$

where e is the magnitude of the charge on the electron. This is the current induced by the applied field E. If the sample has length l, then the voltage applied across the it is $V = El$, and so

$$I = (n\mu_e + p\mu_h)e(V/l)A \tag{8.3.2}$$

The conductance of the detector is then given by the equation

$$C_d = (I/V) = (n\mu_e + p\mu_h)e(A/l) \tag{8.3.3}$$

The voltage across the detector is given by

$$V_d = I/C_d \tag{8.3.4}$$

In a current-biased configuration the current I is held constant, and so the variation of output voltage with changes in the conductivity of the photoconductor is

$$\frac{dV_d}{dC_d} = -I/C_d^2 = -V_d/C_d \tag{8.3.5}$$

If a photon flux Φ falls on the detector, the carrier densities of holes and electrons change by amounts Δp, Δn respectively, where, since incident photons produce electron-hole pairs, $\Delta p = \Delta n$. We also assume, following Mason [5], that

$$\mu_e >> \mu_h\,.$$

It follows that the corresponding change in conductance is

$$\Delta C_d = \frac{A}{l}\mu_e e\Delta p = \left(\frac{1}{l^2}\right)\mu_e e\eta\Phi\tau \tag{8.3.6}$$

using Equation (4.17).

Substituting in (8.3.5) and using $E_d = (V_d/l)$ we obtain

$$\Delta V_d = \frac{\eta e\mu_e E\Phi}{l} R_d\tau$$

This is equation (4.18).